Volatile Organic Compounds (VOCs) Removal from Indoor Air by Heterostructures/Composites/Doped Photocatalysts: A Mini-Review

Alexandru Enesca * and Cristina Cazan

Product Design, Mechatronics and Environmental Department, Transilvania University of Brasov, Eroilor 29 Street, 35000 Brasov, Romania; c.vladuta@unitbv.ro

* Correspondence: aenesca@unitbv.ro; Tel.: +40-732-71-2472

check for updates

Abstract: The impact of volatile organic compounds (VOCs) on indoor air quality and, furthermore, on human health is still a subject of research investigations considering the large increase in forms of cancer and related diseases. VOCs can be 10 times higher in indoor air concentrations then that of the outdoors, as a consequence of emissions from electronics, building materials and consumer goods. Direct transformation of VOCs in mineralization products seems to be an alternative to reduce indoor air contaminants. The advantage of photocatalysis implementation in indoor air treatment is given by the absence of additional chemicals (such as H_2O_2) and waste. The present mini-review presents a comparative study on VOCs photocatalytic removal considering the photocatalyst composition, morphology and specific surface. The sheet-like morphology seems to provide a higher number of active sites which may contribute to oxidative reactions. The insertion of materials able to increase light absorbance or to mediate the charge carrier's transport will have a beneficial impact on the overall photocatalytic efficiency. Additionally, surface chemistry must be considered when developing photocatalysts for certain gas pollutants in order to favor molecule absorbance in the interfacial region. An energy consumption perspective is given based on the light intensity and irradiation period.

Keywords: photocatalysis; heterostructures; composites; indoor air; volatile organic compounds

1. Introduction

Keeping high standards of indoor air quality parameters is a challenge considering that 80% is the average proportion of time individuals spend inside confined spaces. Based on geographical position and economic development, indoor air quality can have worse parameters than outdoor air. There are various categories of indoor air pollutants: CO_x, NO_x, small particles, volatile organic compounds (VOCs), etc. [1–3]. Among them, VOCs can reach ten times higher concentrations indoors than outdoors, as a consequence of emissions from electronics, building materials and consumer goods [4–6].

One way to deal with this issue is preventing pollution by source, but the economic repercussions of this measure on industry and economic development have delayed the practical implementation [7,8]. Instead, additional measures have been considered for reducing the impact of VOCs on human health: increased ventilation or absorbance in filters. The implications of these actions are controversial since they transfer the pollutants from one phase/space to another [9–11].

Direct transformation of VOCs in mineralization products seems to be an alternative to reduce indoor air contaminants [12,13]. Several advanced oxidation processes (AOPs) with good prospects for developing air cleaning technologies were considered: UV/ozonation [14–16], H_2O_2/ozonation [17–19] or photocatalysis [20–22]. The advantage of photocatalysis implementation in indoor air treatment is given by the absence of additional chemicals (such as H_2O_2).

This mini-review explores the possibilities of using a photocatalysis process to eliminate VOCs that are dangerous to human health, such as: toluene, *N,N*-dimethylformamide, acetone, dimethyl fumarate, formaldehyde, benzene, ethylbenzene, o-xylene, acetaldehyde, acetylene, 2-ethyl-1-hexanol, *N*-decane, *N*-hexane, benzaldehyde and trichloroethylene. The influence of photocatalyst composition, morphology, specific surface and light spectra on the photocatalytic efficiency was evaluated. The energy consumption based on light intensity and irradiation period was compared with the amount of pollutant removal. The photocatalytic efficiency refers to partial or total pollutant degradation according to the information provided in the literature. Due to the arbitrary reported photocatalysis experimental parameters and the lack of standardization, the scientific literature is abundant with investigations based on various input data that are difficult to compare.

2. Photocatalysis Mechanisms for VOCs Removal

The morphological properties have an important influence on the photocatalytic efficiency and are considered as the main driving force for photocatalysis processes in the gas phase. The low mass transfer resistance encountered in gas phase photocatalysis can be useful to develop high surface area photocatalysts [23–25]. Another important prerequisite in gas phase photocatalysis, besides large specific surface area and adsorption capacity, is represented by the high photon conversion efficiency [26]. These are the reasons why researchers have worked on developing complex structures (heterostructures, composites, doped materials, etc.) able to convert extended UV–Vis (and even Infrared (IR)) spectra as well as to efficiently use the incident photons for the photogeneration of free charge carriers [27–29].

For pollutants in the gaseous phase, the net mass transfer from the bulk to the external surface of the photocatalyst has a significant impact on the overall efficiency and the rate of reaction. Figures 1–3 illustrate the photocatalytic mechanism of acetaldehyde degradation using a p-n heterostructure. The photocatalytic degradation of VOCs can be induced by employing heterostructures or composites following type II, Schottky, Z-scheme or S-scheme mechanisms. Using multi-component photocatalysts is a suitable method to increase the charge carrier's concentration and consequently the number of photogenerated oxidative species.
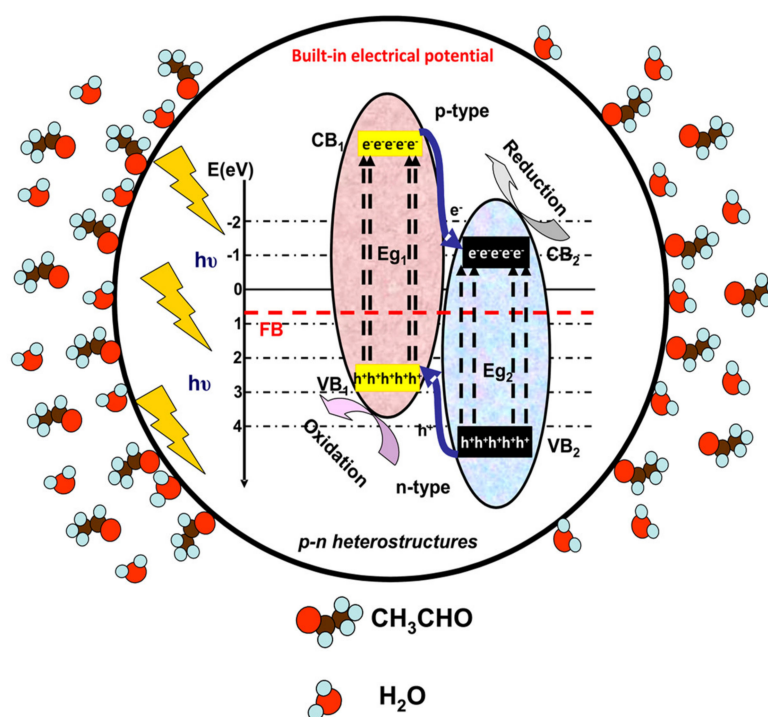

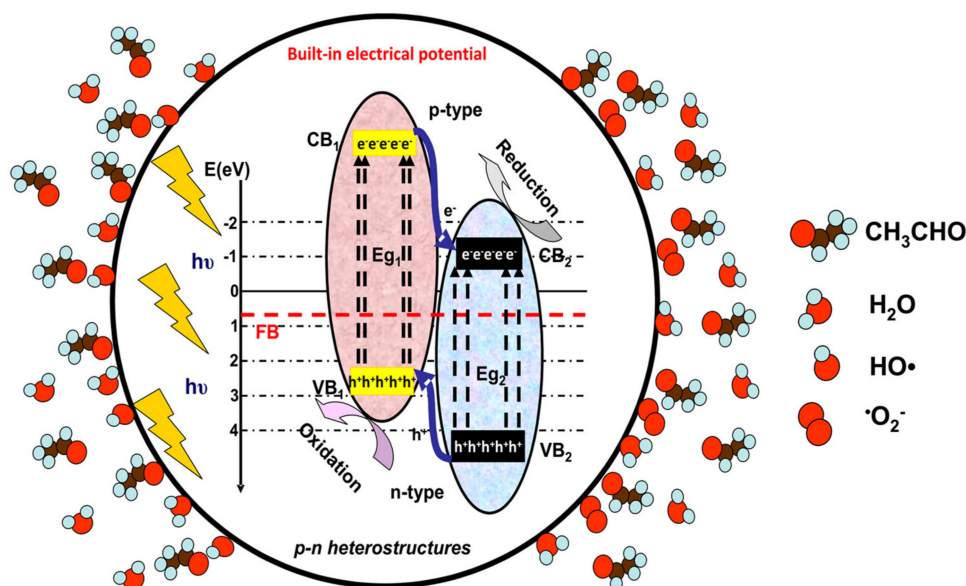**Figure 1.** Charge carrier photogeneration during the initial irradiation period.

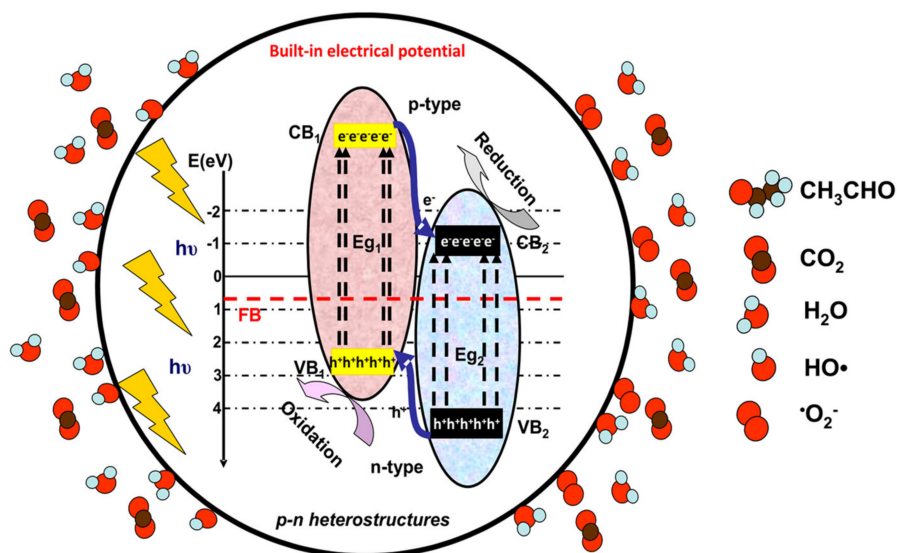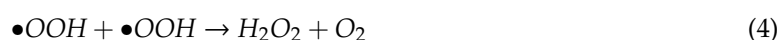**Figure 2.** Development of oxidative and superoxidative species.

Figure 3. Photocatalytic degradation of acetaldehyde gas.

The development of inherent electric fields between the heterostructure partners induces a shift in individual Fermi levels, finally settling on a uniform value [30,31]. The gas molecules and the photocatalysts may the change function of the specific applications envisaged by researchers. The first step is represented by reaching the adsorption-desorption equilibrium in the absence of light irradiation. The duration depends on the surface chemistry between the gas molecules and catalysts as well as the catalyst porosity [32].

Under irradiation (step 2, Figure 1), the p-n heterostructure system generates charge carriers (e^- and h^+) which move toward the surface and support (step 3, Figure 2) the formation of oxidative ($\bullet OH$) or superoxidative ($\bullet O_2^-$) species. Pollutant molecules subsequently adsorb and diffuse into the catalyst pores (step 4, Figure 3), where they react with highly reactive radical species and form compounds with lower molecular weights (H_2O, CO_2 and other intermediate products) [33–35].

The generally accepted reaction mechanism for organic pollutant photodegradation involves a radical pathway [36]. However, the direct oxidation of adsorbed organic pollutants by photogenerated holes has been reported [37,38]. The photocatalytic chain reaction is initiated by the hydroxyl radical

formation ($\bullet OH$) from H_2O (+2.27 V vs. SHE), along with superoxide anion radical formation ($\bullet O_2^-$) from O_2 (-0.28 V vs. SHE), with the involvement of photogenerated h^+ and e^-. Hydroperoxyl radicals ($\bullet OOH$) and H_2O_2 can form due to subsequent reactions of $\bullet O_2^-$ with h^+. Total VOCs mineralization is the goal of the photocatalytic applications. Unfortunately, many studies indicate the occurrence of partial organic pollutant oxidation, which may induce the formation of other pollutant molecules. The optimization of photocatalyst materials and photocatalytic parameters is a pre-requisite to improve the VOCs degradation efficiency [39,40].

$$H_2O + h_{VB}^+ \rightarrow \bullet OH + H \tag{1}$$

$$O_2 + e_{CB}^- \rightarrow \bullet O_2^- \tag{2}$$

$$\bullet O_2^- + H^+ \rightarrow \bullet OOH \tag{3}$$

$$\bullet OOH + \bullet OOH \rightarrow H_2O_2 + O_2 \tag{4}$$

$$H_2O_2 + e_{CB}^- \rightarrow \bullet OH + HO^- \tag{5}$$

3. VOC Removal Using Heterostructures/Composites/Doped Photocatalysts

Several VOCs with negative impacts on human health have been considered for this mini-review. Table 1 contains the key parameters presented in the scientific literature that may influence the photocatalytic activity of the samples. However, there are many other papers and parameters which are not presented here but can have an important impact in this field. Modified photocatalysts have the advantage of enhanced photocatalytic activity based on the insertion of dopant ions or by coupling with other materials. Most of these changes involve the optimization of intrinsic properties based on the energetic levels of the photocatalysts.

3.1. Toluene Photocatalytic Removal

Toluene is considered as an important VOC pollutant with major health hazard implications for the human body. Some of the short-term exposure symptoms to toluene are eye and nose irritation, weakness, exhaustion, confusion, etc. [41,42]. Long-term exposure to toluene induces central nervous system, respiratory system, liver and kidney damage [43]. Using a 300 W Vis light source, two heterostructures developed by in situ growth (TiO_2-MIL-101(Cr) [44]) and hydrothermal (CoO/WO_3 [45]) methods were employed for photocatalytic removal of toluene. TiO_2-MIL-101(Cr) with an octahedral particle morphology and a high specific surface (2128 m^2/g) was tested in 1000 ppm toluene for a 480 min irradiation period in order to achieve 50% photocatalytic efficiency. A CoO/WO_3 p-n heterostructure with a plate-shaped morphology was used as a photocatalyst in 500 ppm toluene and the irradiation period was 240 min. The energy consumption is lower for CoO/WO_3 using 1200 Wh to remove 427 ppm toluene due to CoO's ability to increase the heterostructure Vis light absorbance. The p-type CoO has a negative enough conduction band (CB) to produce more active species, like superoxide radicals. Therefore, it is recommended that the p-type band position of CoO is well matched with that of n-type WO_3. In this way, it is possible to efficiently suppress the recombination of photogenerated charge carriers, thereby enhancing the photocatalytic performance. Using a TiO_2-MIL-101(Cr) heterostructure, it was possible to remove 500 ppm toluene but with the expense of 2400 Wh. The 50% photocatalytic efficiency was obtained based on the synergy effect between two heterojunctions (type II and surface heterojunctions) at the interface contact region of the semiconductors.

Keeping the same intensity (300 W) but changing the light spectra to the UV region, the $CaCO_3/TiO_2$ [46] photocatalytic activity was evaluated at 50 ppm toluene. A $CaCO_3/TiO_2$ heterostructure with an irregular particle morphology obtained by the dip-coating method have the advantage of improved gas molecule adsorption due to the $CaCO_3$ surface chemistry. After 60 min of irradiation, the photocatalytic efficiency was 90%, which represents a 45 ppm toluene reduction with an energy

consumption of 300 Wh. By increasing the UV light intensity up to 500 W, the Ag/TiO$_2$ [47] Schottky junction heterostructure (see Figure 4) exhibits 99.6% photocatalytic efficiency toward 2.6 ppm toluene after a 180 min irradiation period. The Schottky junction develops at the semiconductor-metal interface and is able to reduce charge carrier recombinations and to promote the increase in semiconductor spectral light absorption. A significant feature of the Schottky junction is represented by the localized surface plasmonic resonance (LSPR) effect. Based on the LSPR, the photocatalysts have good visible light absorption and a significant excitation of active electron/hole pairs. The LSPR is present when the metal work function surpasses that of the semiconductor, inducing a positive space-charge region on the photocatalyst surface as well as upward semiconductor bands. The energy consumption is relatively high, considering that 1500 Wh were required to remove 2.59 ppm toluene. A Ag/TiO$_2$ heterostructure with a nanotube morphology obtained by photoreduction was also employed to remove 3.3 ppm *N,N*-dimethylformamide (92.5% photocatalytic efficiency), 4.2 ppm acetone (99.4%) and 1.7 ppm dimethyl fumarate (99.7%). In all cases, the photocatalytic efficiency was high due to the nanotube structures allowing a facile diffusion of gaseous molecules and exposure to active sites. The Schottky junction based on the Ag nanoparticles' uniform distribution inside the bottom-opening titania nanotubes contribute additional charge carriers required to obtain the oxidative species.
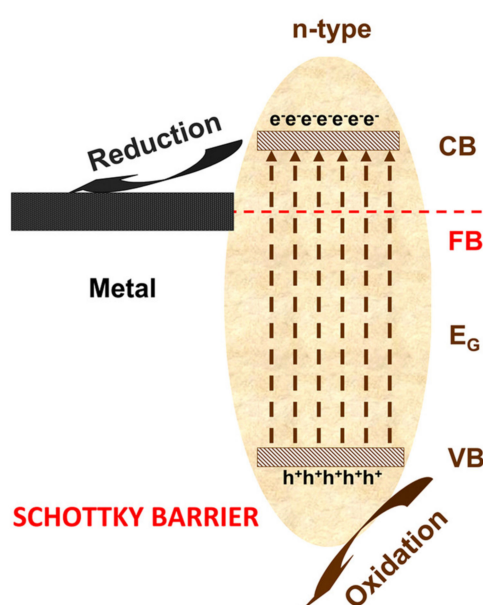

Figure 4. Schottky junction mechanism.

A comparative study regarding the influence of light spectra on the 45.5 ppm toluene removal was done using a TiO$_2$@MgAl [48] heterostructure with a 94.71 m^2/g specific surface. A TiO$_2$@MgAl heterostructure with a plate-like morphology was obtained by the in situ hydrolysis method. The photocatalytic activity was tested in the presence of a 500 W simulated sunlight source and in real sunlight during a 180 min irradiation period. In both situations, the photocatalytic efficiency was relatively high (91.7% in real sunlight and 85.9% in simulated sunlight), with an energy consumption of 1500 Wh to remove 39 ppm toluene (simulated sunlight). The photocatalytic activity was enhanced by the large plate surface area and the ionization ability of metals ions in the presence of water molecules. Another comparative study was done on a WO$_3$/TiO$_2$ type II heterostructure [49] by changing the top and bottom layers (WO$_3$/TiO$_2$ and TiO$_2$/WO$_3$) or by applying a bias (0.2 V). The heterostructures were obtained by the screen printing technique to make films with a 20 μm thickness. The photocatalytic experiments were done in 250 ppm toluene under 5 mW/cm^2 irradiance for a 30 min period. The results indicate a 2.85 times higher photocatalytic activity for WO$_3$/TiO$_2$ (40%) compared to TiO$_2$/WO$_3$ (14%) and almost double the photocatalytic efficiency (70% for WO$_3$/TiO$_2$) when applying a 0.2 V bias. In the

presence of an external bias voltage, the photogenerated electrons can be drawn away via the external circuit, leaving the photogenerated holes for toluene mineralization. For the WO_3/TiO_2 heterostructure, the photogenerated electrons in the CB of TiO_2 could migrate to the CB of WO_3. The electrons could be easily orientated to the external circuit through the WO_3 layer at a low voltage, which acts as an unimpeded conduction passageway for charge carrier migration.

3.2. Photocatalytic Removal of Formaldehyde and O-xylene

Low concentrations of formaldehyde in air (0.1 ppm) produce burning sensations in the eyes and throat, nausea and skin irritation [50,51]. Long-term exposure to formaldehyde may cause severe diseases such as leukemia or cancer of the nasal sinuses [52,53]. The photocatalytic removal of formaldehyde was tested under Vis irradiation using graphene oxide GO/MnO_x/Carbon Nanotubes (CNs) [54] and CeO_2@layered double hydroxide (LBH) [55] heterostructures. GO/MnO_x/CNs exhibit a sheet-like morphology with a bumpy surface structure and enhanced light absorption due to the scattering effect. The heterostructure reaches 90% photocatalytic efficiency for 160 ppm formaldehyde after 12 min of irradiation with a 300 W Vis light source. The GO/MnO_x/CN heterostructures benefit from the improved synergetic photothermocatalysis and photocatalysis effects on decomposing HCHO. The mechanism rapidly enhances the surface temperature of photocatalysts under Vis irradiation and then drives the thermocatalysis of MnO_x. The use of 2D/2D/2D nanosheet assembly increases the charge carrier transfer mechanism and well as the mobility between the sheet-like structures. Based on the temperature variation, the oxygen atom lattice can be activated in order to promote the transfer of photogenerated charge carriers to the carbon nitrate surface and the subsequent surface reactions. The results indicate an optimum energy consumption of 60 Wh to remove 144 ppm formaldehyde. Higher energy consumption was reported for CeO_2@LBHs, which require 2500 Wh to remove 22.6 ppm formaldehyde. CeO_2@LBHs were obtained by the hydrothermal method and have a petal-like lamella morphology, inducing a large specific surface (93 m^2/g). The heterostructure follows a Z-scheme heterojunction mechanism where the photogenerated electrons on the conduction band of CeO_2 are transferred to the valence band of CoAl-LDHs.

The main effect of inhaling o-xylene is depression of the central nervous system, with symptoms such as dizziness, headache or vomiting [56,57]. Chronic exposure may lead to insomnia, tremors, short-term memory loss and impaired concentration [58,59]. Reduced graphene oxide $rGO-TiO_2$ [60] with a sheet-like morphology was obtained by the solvothermal method and contains TiO_2 particles with 8–10 nm diameters. The photocatalytic activity was evaluated toward 25 ppm o-xylene using a 200 W Vis light source and a 160 min irradiation period. The results indicate a 54% photocatalytic efficiency at 533.3 Wh of energy consumption. A similar experiment involving $rGO-TiO_2$ [60] was done with 25 ppm acetaldehyde and the photocatalytic efficiency was 42%. In this case, with the same energy consumption (533.3 Wh), the quantity of pollutant removal was lower (10.5 ppm reduction). When rGO is combined with titania, the specific surface area (227.3 m^2/g) and the π–π bonds in graphene improve the organic compound adsorption. The decrease in intermolecular potential energy, which facilitates the adsorption process, is a consequence of dipole-dipole interactions between the rGO and the pollutant. The π-electron-rich active sites of rGO present a high affinity toward o-xylene molecules, which explains the enhanced photocatalytic activity from the initial stage. In the composite material, some of the electrons were trapped by the rGO sheet defects, prolonging the lifetime of the holes.

3.3. Photocatalytic Removal of Benzene and Ethylbenzene

Long-term exposure to benzene (and related compounds such as ethylbenzene, phenol, benzaldehyde, etc.) has been associated with a wide range of chronic health effects, including aplastic anemia (bone marrow is no longer able to produce enough red blood cells) and various forms of cancer [61,62]. Additionally, it can damage the immune system due to changes in the level of antibodies in the blood [63]. UV light with a 300 W intensity (TiO_2/porous cementitious (PC) material [64]) and Vis light with a 100 W intensity (Cu-$NiWO_4$ [65]) were employed to evaluate the photocatalytic

removal of benzene. TiO$_2$/PC was obtained by the negative pressure co-stirring method and exhibited a porous morphology with a 26 m^2/g specific surface. The photocatalytic activity was evaluated for the removal of 200 ppm benzene during 180 min of UV irradiation. Low-density PC materials are useful to disperse the loaded titania particles due to the loose network of pores of needle-like hydrates, while the high-density substrates induce the agglomeration of loaded TiO$_2$ particles. The photocatalytic efficiency was 63%, which represents 900 Wh of energy consumption to remove 126 ppm benzene. A Cu-NiWO$_4$ heterostructure uses 4.5 times less energy (200 Wh) to remove 2.6 times less benzene (48.25 ppm). The presence of a Cu dopant induces the formation of medium-band energy between the conduction band and valence band of NiWO$_4$, effectively reducing the electron–hole recombination rate. Based on the Cu dopant concentration, the photogenerated charge carriers have enough reduction or oxidation potential to react with oxygen and water molecules to form oxidative species. In this case, the high photocatalytic efficiency (96.5%) under 100 W Vis light source irradiation for 120 min was attributed to a high concentration of oxygen defects, inducing an increase in the benzene adsorption.

A BiVO$_4$/TiO$_2$ type II heterostructure [66] was employed for the evaluation of the influence of light spectra on the 260 ppm removal of benzene. Type II heterostructures (see Figure 5) are characterized by a potential difference formed between two semiconductors which separate the photogenerated charge carriers and prevent recombination processes. The reason is that the energy bands of one semiconductor have higher values compared to those of the second semiconductor. In this way, there is an effective separation between the holes and electrons on both sides.
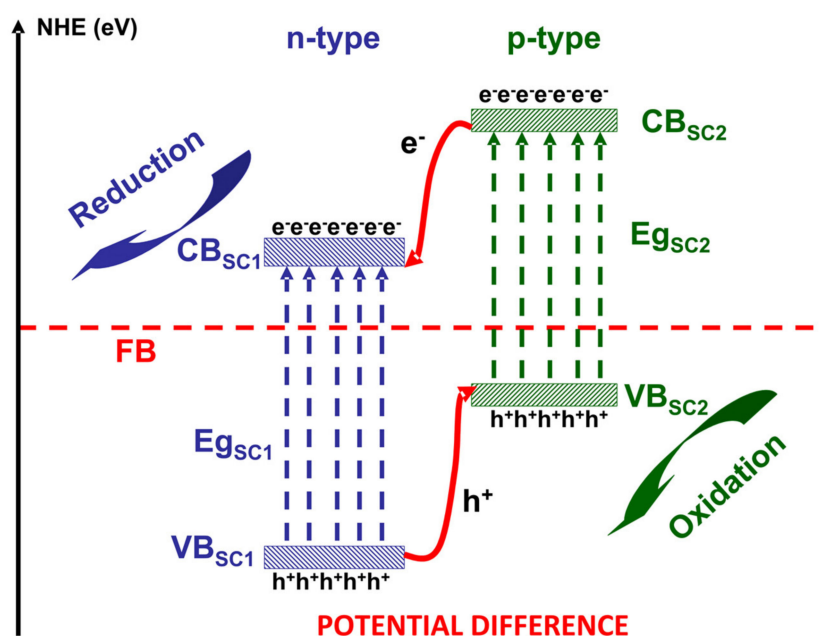

Figure 5. Type II heterostructure mechanism.

A heterostructure with irregular particles was obtained by the hydrothermal method and was irradiated with 500 W solar simulated light, Vis and UV sources for 480 min. For the same energy consumption (~4000 Wh), the benzene removal in solar simulated light (240 ppm reduction) and Vis light (173.6 ppm reduction) was significantly higher compared to UV light (28.6 ppm reduction) irradiation. The photocatalytic activity uses BiVO$_4$ as a sensitizer for the visible light-induced redox process, while TiO$_2$ represents the substrate. Because BiVO$_4$ is considered as an intrinsic semiconductor, its Fermi level lies in the middle of the conduction band and valence band.

Low-intensity UV radiation sources were used to determine the photocatalytic properties of SnO_x/Zn_2SnO_4 [67] and $Fe-TiO_2$ [68] samples. A SnO_x/Zn_2SnO_4 heterostructure with rods (5 nm diameter and 100 nm length) and flake-like particles and a 21.7 m^2/g specific surface was obtained by the hydrothermal method. After 840 min of irradiation with a 9 W UV source, the photocatalytic efficiency reached 80.3%. The benzene concentration was reduced to 200 ppm from 250 ppm using only 126 Wh of energy. SnO_x/Zn_2SnO_4 follow a type II heterojunction mechanism, where the photogenerated electrons transfer from SnO_2 to Zn_2SnO_4 due to the energy offset, while the photogenerated holes migrate from the valence band (VB) of Zn_2SnO_4 to the VB of SnO_2. A similar study was done using a 8 W UV source to irradiate $Fe-TiO_2$ nanoparticles for only 5 min. The authors [68] used a low benzene concentration (0.1 ppm), and the photocatalytic efficiency was 33%, which corresponds to the removal of 0.033 ppm with 0.66 Wh of energy consumption. $Fe-TiO_2$ photocatalytic activity was also evaluated for toluene, ethylbenzene and o-xylene using the same VOC concentration and setup parameters. The photocatalytic efficiency varied from 68% for toluene to 83% for ethylbenzene and 91% for o-xylene due to the surface absorbance specificity for certain molecules. Additionally, Fe^{3+} species could act as electron and hole traps, reducing charge carrier recombination and improving photocatalytic performance. The excess doping of TiO_2 with transition metals could increase the number of electron-hole recombination centers or even completely block the reaction sites. This process will drastically reduce the photocatalytic activity and this can be prevented by controlling the amount of transition metals related to the photocatalyst crystalline structure and composition. Higher photocatalytic efficiency (99%) for 11.5 ppm ethylbenzene was obtained by UV irradiation of $La-TiO_2$ [69] for 1 min. $La-TiO_2$ was obtained by combining the sol-gel and hydrothermal methods. The significant improvement of the photocatalytic efficiency corresponding to 1.2% La^{3+} doping may be attributed to the tubular structure and large surface area of nanotubes (541.35 m^2/g), inducing homogenous reactant adsorption.

3.4. Acetaldehyde Photocatalytic Removal

Acetaldehyde is usually considered as an intermediate in the chemical synthesis of different products. Short-term exposure induces symptoms including irritation of the skin, respiratory tract and eyes [70,71]. Long-term exposure may be responsible for laryngeal or nasal cancerous tumors [72,73]. The photocatalytic activity of $rGO-TiO_2$ [74] and TiO_2/TaS_2 [75] was evaluated under a 260 W Vis light source using 500 ppm acetaldehyde. The $rGO-TiO_2$ with a sheet-like morphology was obtained by the ultrasonication method. After 60 min of irradiation, the photocatalytic efficiency was 80%, corresponding to a 400 ppm reduction with 260 Wh of energy consumption. Compared with $rGO-TiO_2$, TiO_2/TaS_2 has a similar morphology and was obtained using the same synthesis method (ultrasonication). However, TiO_2/TaS_2 exhibited a higher photocatalytic efficiency (98%) due to a longer exposure period (65 min vs. 60 min) and a higher specific surface (103 m^2/g vs. 69.81 m^2/g). The energy consumption for a 490 ppm acetaldehyde reduction was 281.6 Wh. TaS_2 provided two merits: (i) the increase in adsorptive capacity (three times bigger than that of TiO_2) and (ii) higher photo-current (four times bigger than that of TiO_2). TaS_2 is considered as a typical two-dimensional material that can be integrated in composite structures or used as contact layer between two semiconductors. An advantage of using TaS_2 is represented by its large specific surface area and low electrical resistivity which are beneficial in gaseous photocatalysis. Additionally, TaS_2 increases the separation efficiency of photogenerated charge carriers.

Keeping the same radiation intensity (260 W) but switching from Vis to UV, the photocatalytic activity of $Ag@TiO_2$ [76] and carbon quantum dots (CQDs)/TiO_2 [77] was evaluated. $Ag@TiO_2$ with a wire-like morphology and a 105.9 m^2/g specific surface was obtained by the solvothermal method. After 4.8 min of irradiation, the sample exhibited 72% photocatalytic efficiency, which represented only 20.8 Wh of energy consumption to remove 360 ppm from 500 ppm acetaldehyde. The excellent photocatalytic activity is based on the Schottky junction, which increases the charge carrier concentration and mobility through the structure. CQDs/TiO_2 with an irregular morphology were obtained by ultrasonication and the photocatalytic tests were done in the same conditions as for

Ag@TiO_2 but the irradiation period was 120 min. The increase in photocatalytic efficiency, up to 99%, was detrimental to the energy consumption, which was bigger (520 Wh) compared to that for Ag@TiO_2. CQDs could serve as electron reservoirs by harvesting and retaining the photogenerated electrons from the conduction band of TiO_2. During UV irradiation, the trapped photogenerated electrons on CQDs could further reduce the absorbed O_2 to superoxidative radicals ($\bullet O_2^-$). If the same sample is irradiated with a 400 W Vis light source for 120 min, the photocatalytic efficiency decreases significantly (30%) due to lower TiO_2 photoconversion.

Highly concentrated acetaldehyde (3000 ppm) was used to evaluate the photocatalytic activity of a SiO_2/TiO_2 [78] type II heterojunction with a 20.5 m^2/g specific surface obtained by the fiber impregnation method. The evaluation was done with and without plasma assistance and the results showed that total pollutant degradation is possible by using 22.6 W UV light source irradiation. The irradiation period is significantly reduced with plasma assistance (90 min) compared to without plasma assistance (140 min). These methods are difficult to compare in terms of energy consumption because the energy saved from the reduced irradiation period is used for plasma production. The reasons for coupling the photocatalysis process with plasma is the fact that plasma treatment interferes with oxidation reactions during the pollutant degradation and generates UV radiation (due to excited nitrogen relaxation), which is beneficial for TiO_2 anatase photocatalytic activity. Additionally, the photocatalysis process can have an important influence on the improvement of carbon dioxide selectivity and mineralization balance.

A double $CuInS_2/TiO_2/SnO_2$ [79] type II and p-n heterojunction was employed to evaluate the photocatalytic properties under UV-Vis irradiation. $CuInS_2/TiO_2/SnO_2$ with a porous morphology (25.3 m^2/g) was obtained by spray pyrolysis deposition. After 720 min of irradiation using a 20 W UV-Vis light source, the photocatalytic efficiency reached 51.7%. $CuInS_2/TiO_2/SnO_2$ benefits from the synergic effect of dual type II and p-n heterojunctions, which allow for simultaneous charge photogeneration at each heterostructure component and lower recombination rates. Consequently, the energy consumption is 240 Wh in order to remove 258.5 ppm acetaldehyde. The photocatalytic efficiency depends on the intimate contact at the interface between components, as well as the surface chemistry in relation to the pollutant molecules. The degradation mechanism is positively influenced by the simultaneous charge carrier photogeneration of the heterostructure components and the increased mobility due to the suitable position of the energy bands.

3.5. Photocatalytic Removal of 2-ethyl-1-hexanol, N-decane, N-hexane, Trichloroethylene and Benzaldehyde

The photocatalytic removal of 2-ethyl-1-hexanol [80] and n-decane [81] was evaluated under Vis irradiation for 300 min. GO/TiO_2 [80] with a sheet-like morphology and a large specific surface (100.3 m^2/g) was obtained by ultrasonication and tested for the removal of low-concentration (0.1 ppm) 2-ethyl-1-hexanol. GOs in GO/TiO_2 under visible light illumination act as sensitizers (electron donors) of titania that transfer the photogenerated electrons from the conduction band of GO/TiO_2, reducing the recombination of photogenerated charge carriers and enabling GO/TiO_2 to work under visible light irradiation. The 99.3% photocatalytic efficiency was obtained with low energy consumption (40 Wh) after 300 min of irradiation with a 8 W Vis light source, however, the initial pollutant concentration was only 0.1 ppm. Cellulose acetate (CA)/TiO_2-P25 [81] with a porous morphology, obtained by the cold spray method, was irradiated with a 1700 W Vis light source to evaluate the photocatalytic removal of 320 ppm n-decane. The experimental investigations indicated that the photocatalytic reaction rate depends on the water/n-decane molar ratio. The competitive adsorption of water on the catalyst surface is favored by high water/n-decane ratios and reduces the adsorption of n-decane molecules, resulting in lower reaction rates. The photocatalytic efficiency was 72% and corresponded to a high energy consumption (8500 Wh for 230.4 ppm reduction).

The accumulation of n-decane and n-hexane indoors from paint and solvents products can induce an increased number of conjuctival polymorphonuclear leukocytes and irritation of the mucous membranes of the eyes [82–84]. Bi/BiOBr [85] with a spherical particle morphology, obtained by the solvothermal method, was employed to evaluate 15 ppm n-hexane removal using a 300 W Vis light source. The Schottky Bi/BiOBr junction greatly inhibits the photogenerated carrier recombination rate, thereby promoting the accumulation of photoinduced electrons and holes in the conduction and valence bands of BiOBr to produce highly concentrated reactive oxygen species. A synthesis method that allows for the simultaneous formation of metallic Bi and BiOBr has the advantage of maintaining the BiOBr structure and imitates the chemical reaction occurring between Bi and BiOBr. The band gap narrowing for improved visible light absorption occurs due to the chemical bonding between Bi and BiOBr. Consequently, the photogenerated charge carriers increase, as well as the Bi/BiOBr composite photocatalytic activity. The photogenerated electron migration occurs from the conduction band of BiOBr to metallic Bi, improving the negative charge accumulation on Bi. This is the pathway to improve the photogenerated charge carrier separation on BiOBr, resulting in a higher charge lifetime. After 120 min of irradiation, the Bi/BiOBr sample exhibited 97.4% photocatalytic efficiency which represented 600 Wh of energy consumption to remove 14.6 ppm n-hexane.

The UV photocatalytic removal of trichloroethylene [86] and benzaldehyde [87] was evaluated with different photocatalytic materials. TiO_2/SiO_2 [86] with a granular morphology and a large specific surface (300 m^2/g) was obtained by the dip-coating method. The photocatalytic activity was evaluated with 26 ppm trichloroethylene for a 240 min irradiation period. The total trichloroethylene removal was a consequence of higher gas affinity on the surface of the silica-based material. SiO_2 particles, with their high surface area, represent a buffer and provide a suitable medium for trichloroethylene accumulation, resulting in higher overall conversion. TiO_2/conductive carbon felt (OMT/CCF) [86] with a fiber-like morphology (148.6 m^2/g specific surface) was obtained by the liquid crystal template method with the assistance of ultrasonic deposition. The photocatalytic removal of 100 ppm benzaldehyde at 40 mW/cm^2 irradiance was tested for a 325 min irradiation period and the photocatalytic efficiency was ~25% due to the synergistic relationship between CCF, which acts as an excellent electron acceptor and organic gas concentrator, and OMT, representing a reactant transporter and reactor, thus reducing the photogenerated charge carrier recombination.

Table 1. Representative studies on photocatalytic applications for volatile organic compound (VOC) removal.

Heterostructure/ Composite/ Doped Photocatalysts	Synthesis Method	Specific Surface (S_{BET})/Radiation Parameter (Light Spectra, Intensity and Irradiance)/Energy Consumption (E_C)	Pollutant/Photocatalytic Parameters	Ref.
TiO_2-MIL-101 (Cr)	In situ growth on MIL101 (Cr)	S_{BET} = 2128 m^2/g300W Vis, np* E_c = 2400 Wh	Toluene Pollutant concentration: 1000 ppm Time: 480 min Efficiency: ~50% Rate constant: np	[44]
CoO/WO_3	Hydrothermal	S_{BET} = np 300W Vis, np E_c = 1200 Wh	Toluene Pollutant concentration:500 ppmTime: 240 min Efficiency: 85.4% Rate constant: 0.0070 min^{-1}	[45]
$CaCO_3$ loading TiO_2	Dip coating	S_{BET} = np 300W UV, 0.29 W/cm^2 E_c = 300 Wh	Toluene Pollutant concentration: 50 ppm Time: 60 min Efficiency: 90% Rate constant: np	[46]

Table 1. *Cont.*

Heterostructure/ Composite/ Doped Photocatalysts	Synthesis Method	Specific Surface (S_{BET})/Radiation Parameter (Light Spectra, Intensity and Irradiance)/Energy Consumption (E_C)	Pollutant/Photocatalytic Parameters	Ref.
Ag/TiO$_2$	Photoreduction method	S_{BET} = np 500 W UV, np E_c = 1500 Wh	Toluene, N,N-dimethylformamide, acetone, dimethyl fumaratePollutant concentration: 2.6 ppm (toluene), 3.3 ppm (N,N-dimethylformamide), 4.2 ppm (acetone), 1.7 ppm (dimethyl fumarate) Time: 180 min Efficiency: 99.6% (toluene), 92.5% (N,N-dimethylformamide), 99.4% (acetone), 99.7% (dimethyl fumarate) Rate constant: np	[47]
TiO$_2$@MgAl-layered double hydroxide	In situ hydrolysis	S_{BET} = 94.71 m^2/g500 W Vis, np Real sunlight, np E_c = 1500 Wh	ToluenePollutant concentration: 45.5 ppm Time: 180 min Efficiency: 91.7% (true sunlight), 85.9% (simulated sunlight) Rate constant: 0.0100 min^{-1}	[48]
WO$_3$/TiO$_2$	Screen printing technique	S_{BET} = np UV, 5 mW/cm^2 E_c = np	Toluene Pollutant concentration: 250 ppm Time: 30 min Efficiency: 14% (T/W), 40% (W/T), 70% (W/T with 0.2 V bias) Rate constant: 0.00739 min^{-1} (T/W), 0.02004 min^{-1} (W/T)	[49]
Graphene oxide (GO)/MnO$_x$/CN	Vacuum filtration	S_{BET} = np 300 W Vis, np E_c = 60 Wh	Formaldehyde Pollutant concentration: 160 ppm Time: 12 min Efficiency:90% Rate constant: 0.202 min^{-1}	[54]
CeO$_2$@ layered double hydroxides	Hydrothermal	S_{BET} = 93 m^2/g500 W Vis, np E_c = 2500 Wh	Formaldehyde Pollutant concentration: 26 ppm Time: 300 min Efficiency: 86.9% Rate constant: 0.00101 min^{-1}	[55]
Reduced graphene oxide (rGO)-TiO$_2$	Solvothermal	S_{BET} = 227.3 m^2/g 200W Vis, np E_c = 533 Wh	Acetaldehyde, o-xylene Pollutant concentration: 25 ppm Time: 160 min Efficiency: 42% (acetaldehyde), 54% (o-xylene). Rate constant: np	[60]
TiO$_2$/porous cementitious material	Negative pressure co-stirring method	S_{BET} = 26 m^2/g 300W UV, 0.96 mW/cm^2 E_c = 900 Wh	Benzene Pollutant concentration: 200 ppm Time: 180 min Efficiency: 63% Rate constant: np	[64]
Cu-NiWO$_4$	Sol-gel	S_{BET} = 12.4 m^2/g 100W Vis, 0.025 W/cm^{2}E$_c$ = 200 Wh	Benzene Pollutant concentration: 50 ppm Time: 120 min Efficiency: 96.5% Rate constant: np	[65]
BiVO$_4$/TiO$_2$	Hydrothermal	S_{BET} = 66.49 m^2/g 500 W solar simulated light, np 500 W Vis, np 500 W UV, np E_c = 4000 Wh	Benzene Pollutant concentration: 260 ppm Time: 480 min Efficiency: 92% (solar simulated light), 66.8% (Vis), 11% (UV) Rate constant: np	[66]

Table 1. *Cont.*

Heterostructure/ Composite/ Doped Photocatalysts	Synthesis Method	Specific Surface (S_{BET})/Radiation Parameter (Light Spectra, Intensity and Irradiance)/Energy Consumption (E_C)	Pollutant/Photocatalytic Parameters	Ref.
SnO_x/Zn_2SnO_4	Hydrothermal	S_{BET} = 21.7 m^2/g 9 W UV, np E_c = 126 Wh	Benzene Pollutant concentration: 250 ppm Time: 840 min Efficiency: 80.3% Rate constant: 0.0834 min^{-1}	[67]
Fe-TiO$_2$	Electrospinning technique	S_{BET} = np8W UV, 0.4 mW/cm^2 E_c = 0.66 Wh	Benzene, toluene, ethylbenzene and o-xylene Pollutant concentration: 0.1 ppm Time: 5 min Efficiency: 33% (benzene), 68% (toluene), 83% (ethylbenzene) and 91% (o-xylene) Rate constant: np	[68]
La-TiO$_2$	Sol–gel method and hydrothermal technique	S_{BET} = 541.35 m^2/g UV, 20.9 mW/cm^2 E_c = np	Ethylbenzene Pollutant concentration: 11.5 ppm Catalyst dosage: 1 min Efficiency: 99% Rate constant: 1.1860 min^{-1}	[69]
Reducend graphene oxide (rGO) with TiO$_2$	Ultrasonication	S_{BET} = 69.81 m^2/g 260 W Vis, np E_c = 260 Wh	Acetaldehyde Pollutant concentration: 500 ppm Time: 60 min Efficiency: 80% Rate constant: np	[74]
TiO$_2$/TaS$_2$	Ultrasonication	S_{BET} = 103 m^2/g 260 W Vis, np E_c = 281 Wh	Acetaldehyde Pollutant concentration: 500 ppm Time: 65 min Efficiency: 98% Rate constant: 0.03091 min^{-1}	[75]
Ag@TiO$_2$	Solvothermal	S_{BET} = 105.93 m^2/g 260W UV, 20 mW/cm^2 E_c = 20.8 Wh	Acetaldehyde Pollutant concentration: 500 ppm Time: 4.8 min Efficiency: 72% Rate constant: 0.01199 min^{-1}	[76]
Carbon quantum dots/TiO$_2$	Ultrasonication	S_{BET} = np 260W UV, 20 mW/cm^2 400W Vis, np E_c = 520 Wh (UV) E_c = 800 Wh (Vis)	Acetaldehyde Pollutant concentration: 500 ppm Time: 120 min Efficiency: 99% (UV), 30% (Vis) Rate constant: np	[77]
SiO$_2$/TiO$_2$	Fiber impregnation	S_{BET} = 20.5 m^2/g 22.6 W UV, 6 mW/cm^2 E_c = 52.7 Wh (photocat) E_c = 34 Wh (plasma photocat)	Acetylene Pollutant concentration: 3000 ppm Time: 140min (photocat), 90 min (plasma photocat) Efficiency: 100% Rate constant: np	[78]
CuInS$_2$/TiO$_2$/SnO$_2$	Spray pyrolysis deposition	S_{BET} = 25.3 m^2/g 20 W UV + Vis, (2.5 mW/cm^2 +0.1 mW/cm^2) E_c = 240 Wh	Acetaldehyde Pollutant concentration: 500 ppm Time: 720 min Efficiency: 51.7% Rate constant: 0.0557 min^{-1}.	[79]
GO/TiO$_2$	Ultrasonication	S_{BET} = 100.3 m^2/g 8 W Vis, np E_c = 40 Wh	2-ethyl-1-hexanol Radiation: Vis Pollutant concentration: 0.1 ppm Time: 300 min Efficiency: 99.3% Rate constant: np	[80]
Cellulose acetate (CA)/TiO$_2$-P25	Cold spray	S_{BET} = np 1700 W Vis, 38.4 W/m^2 E_c = 8500 Wh	N-decane Pollutant concentration: 320 ppm Time: 300 min Efficiency: 72% Rate constant: np	[81]

Table 1. *Cont.*

Heterostructure/ Composite/ Doped Photocatalysts	Synthesis Method	Specific Surface (S_{BET})/Radiation Parameter (Light Spectra, Intensity and Irradiance)/Energy Consumption (E_C)	Pollutant/Photocatalytic Parameters	Ref.
Bi/BiOBr	Solvothermal	S_{BET} = np 300 W Vis, np E_c = 600 Wh	N-hexane Pollutant concentration: 15 ppm Time: 120 min Efficiency: 97.4% Rate constant: 0.0300 min^{-1}	[85]
TiO$_2$/SiO$_2$	Dip coating	S_{BET} = 300 m^2/g UV (254 nm and 365 nm) Ir_{254} = 7.3 × 10^{-3} W/cm^2 Ir_{365} = 3.5 × 10^{-3} W/cm^2 E_c = np	Trichloroethylene Pollutant concentration: 26 ppm Time: 240 min Efficiency: 100% Rate constant: np	[86]
Mesoporous TiO$_2$/conductive carbon felt (OMT/CCF)	Liquid crystal template method with the assistance of ultrasonic deposition	S_{BET} = 148.6 m^2/g UV, 40 mW/cm^2 E_c = np	Benzaldehyde Pollutant concentration: 100 ppm Time: 325 min Efficiency: ~25% Rate constant: 0.0004 min^{-1}	[87]

* not provided.

Finding new and innovative solutions to enhance the photocatalytic properties is a pre-requisite in consolidating AOPs as future alternatives for VOCs removal. It was found that doping TiO$_2$ with Mn^{2+} or Co^{2+} [88] can increase the photocatalytic activity due to morphological changes, inducing a higher absorbance capability, and can shift the band gap toward the Vis range. Bismuth-doped titania [89], as well as eosin-modified TiO$_2$ [90], were reported to have high photocatalytic activity due to intrinsic property changes, such as oxygen vacancy formation or light trapping. Titania, especially the anatase form, seems to be one of the most suitable photocatalysts, with high chemical stability and versatile morphologies. However, the main disadvantage is represented by the limited absorption in the UV range, which reduces the quantity of photons able to participate in the photocatalytic reactions. Processes like doping or coupling with other materials represent a suitable solution to improve the TiO$_2$ absorption range and the overall photocatalytic efficiency. Based on the literature review, there is no specific photocatalyst that can be recommended for a certain pollutant molecule. Highly active photocatalysts can act indiscriminately on organic pollutants with several specifications: interface compatibility, concentration range and light spectral absorbance. There are specific ways to improve the overall photocatalytic efficiency, which depends on materials (monocomponent, multicomponent, doped, etc.) and process (mechanism, radiation type, intensity, etc.).

4. Conclusions

The real impact of VOCs in indoor air on human health is still a subject of research investigations considering the large increase in forms of cancer and related diseases. The implementation of modern materials and technologies in houses and workspaces has induced the increased concentration and diversification of VOCs. While waiting for health impact studies, prevention should be considered. Photocatalysis may represent a safe method to eliminate VOCs if complete pollutant mineralization occurs.

The photocatalytic efficiency for VOC removal depends not only on the photocatalyst composition but also on the morphology and specific surface. A sheet-like morphology seems to provide a larger number of active sites, which may contribute to the oxidative reactions. The insertion of materials able to increase light absorbance or to mediate the charge carrier transport will have a beneficial impact on the overall photocatalytic efficiency. Additionally, surface chemistry must be considered when developing photocatalysts for certain gas pollutants in order to favor molecule absorbance in the interfacial region.

Energy sustainability for future large-scale implementation requires significantly more experimental investigations. The scientific literature is abundant in various but rather non-uniform correlations regarding the energy demand for photocatalytic pollutant removal. There are studies which use high energy consumption to remove small quantities of pollutants or papers giving incomplete data on this subject. Standardization should be considered as a useful tool to compare and improve the research results in this field considering the high impact on human health. Nevertheless, the development of new photocatalytic materials or technologies, such as coupling photocatalysis with other techniques (adsorption, biodegradation, etc.), can be another pathway to follow for optimum energy consumption and organic pollutant removal.

References

1. Xia, T.; Chen, C. Evolution of pressure drop across electrospun nanofiber filters clogged by solid particles and its influence on indoor particulate air pollution control. *J. Hazard. Mater.* **2020**, *402*, 123479. [CrossRef] [PubMed]

2. O'Lenick, C.R.; Wilhelmi, O.V.; Michael, R.; Hayden, M.H.; Baniassadi, A.; Wiedinmyer, C.; Monaghan, A.J.; Crank, P.J.; Sailor, D.J. Urban heat and air pollution: A framework for integrating population vulnerability and indoor exposure in health risk analyses. *Sci. Total Environ.* **2019**, *660*, 715–723. [CrossRef] [PubMed]

3. Taylor, J.; Shrubsole, C.; Symonds, P.; Mackenzie, I.; Davies, M. Application of an indoor air pollution metamodel to a spatially-distributed housing stock. *Sci. Total Environ.* **2019**, *667*, 390–399. [CrossRef] [PubMed]

4. Shah, K.W.; Li, W. A Review on Catalytic Nanomaterials for Volatile Organic Compounds VOC Removal and Their Applications for Healthy Buildings. *Nanomaterials* **2019**, *9*, 910. [CrossRef] [PubMed]

5. Chi, C.; Chen, W.; Guo, M.; Weng, M.; Shen, X. Law and features of TVOC and Formaldehyde pollution in urban indoor air. *Atmos. Environ.* **2016**, *132*, 85–90. [CrossRef]

6. Barron, M.; Torero, M. Household electrification and indoor air pollution. *J. Environ. Econ. Manag.* **2017**, *86*, 81–92. [CrossRef]

7. Jeleńska, M.; Górka-Kostrubiec, B.; Werner, T.; Kądziałko-Hofmokl, M.; Szwarczewski, P. Evaluation of indoor/outdoor urban air pollution by magnetic, chemical and microscopic studies. *Atmos. Pollut. Res.* **2017**, *8*, 754–766. [CrossRef]

8. Ding, J.; Wang, H.; Luo, Y.; Xu, Y.; Liu, J.; Lin, Y. (002) Oriented $Bi_2O_2CO_3$ Nanosheets with Enhanced Photocatalytic Performance for Toluene Removal in Air. *Catalysts* **2020**, *10*, 389. [CrossRef]

9. Ruan, T.; Rim, D. Indoor air pollution in office buildings in mega-cities: Effects of filtration efficiency and outdoor air ventilation rates. *Sustain. Cities Soc.* **2019**, *49*, 101609. [CrossRef]

10. Adamová, T.; Hradecký, J.; Prajer, M. VOC Emissions from Spruce Strands and Hemp Shive: In Search for a Low Emission Raw Material for Bio-Based Construction Materials. *Materials* **2019**, *12*, 2026. [CrossRef]

11. Ke, S.; Liu, Q.; Deng, M.; Zhang, X.; Sui, G. Cytotoxicity analysis of indoor air pollution from biomass combustion in anmal keratinocytes on a multilayered dynamic cell culture platform. *Chemosphere* **2018**, *208*, 1008–1017. [CrossRef] [PubMed]

12. Yu, S.; Yu, Z.; Ma, X.; Zhang, G.; Feng, G. Study on the influence of pollution source location on indoor pollutant distribution under different air supply. *Proc. Eng.* **2017**, *205*, 2623–2630. [CrossRef]

13. Zadi, T.; Azizi, M.; Nasrallah, N.; Bouzaza, A.; Assadi, A.A. Indoor air treatment of refrigerated food chambers with synergetic association between cold plasma and photocatalysis: Process performance and photocatalytic poisoning. *Chem. Eng. J.* **2020**, *382*, 122951. [CrossRef]

14. Saoud, W.A.; Assadi, A.A.; Kane, A.; Jung, A.V.; Wolbert, D. Integrated process for the removal of indoor VOCs from food industry manufacturing: Elimination of Butane-2,3-dione and Heptan-2-one by cold plasma-photocatalysis combination. *J. Photochem. Photobiol. A* **2020**, *386*, 112071. [CrossRef]

15. Kulathunga, K.M.; Yan, C.F.; Bandara, J. Photocatalytic removal of airborne indoor pollutants by IR illuminated silver coated TiO₂ catalyst: Advantage of one-dimensional TiO₂ nanostructures in IR active photocatalysis. *Colloid. Surf. A* **2020**, *590*, 124509. [CrossRef]

16. Dong, F.; Zhang, P.; Li, K.; Liu, X.; Zhang, P. Nano Copper Oxide-Modified Carbon Cloth as Cathode for a Two-Chamber Microbial Fuel Cell. *Nanomaterials* **2016**, *6*, 238. [CrossRef]

17. Jo, W.K.; Park, K.H. Heterogeneous photocatalysis of aromatic and chlorinated volatile organic compounds (VOCs) for non-occupational indoor air application. *Chemosphere* **2004**, *57*, 555–565. [CrossRef]

18. Dundar, I.; Krichevskaya, M.; Katerski, A.; Krunks, M.; Oja Acik, I. Photocatalytic Degradation of Different VOCs in the Gas-Phase over TiO₂ Thin Films Prepared by Ultrasonic Spray Pyrolysis. *Catalysts* **2019**, *9*, 915. [CrossRef]

19. Karafas, E.S.; Romanias, M.N.; Stefanopoulos, V.; Binas, V.; Papagiannakopoulos, P. Effect of metal doped and co-doped TiO₂ photocatalysts oriented to degrade indoor/outdoor pollutants for air quality improvement. A kinetic and product study using acetaldehyde as probe molecule. *J. Photochem. Photobiol. A* **2019**, *371*, 255–263. [CrossRef]

20. Enesca, A.; Andronic, L.; Duta, A. The influence of surfactants on the crystalline structure, electrical and photocatalytic properties of hybrid multi-structured (SnO₂, TiO₂ and WO₃) thin films. *Appl. Surf. Sci.* **2012**, *258*, 4339–4346. [CrossRef]

21. Lee, J.Y.; Choi, J.-H. Sonochemical Synthesis of Ce-doped TiO₂ Nanostructure: A Visible-Light-Driven Photocatalyst for Degradation of Toluene and O-Xylene. *Materials* **2019**, *12*, 1265. [CrossRef] [PubMed]

22. Nath, R.K.; Zain, M.F.M.; Jamil, M. An environment-friendly solution for indoor air purification by using renewable photocatalysts in concrete: A review. *Renew. Sustain. Energ. Rev.* **2016**, *62*, 1184–1194. [CrossRef]

23. Verbruggen, S.W. TiO₂ photocatalysis for the degradation of pollutants in gas phase: From morphological design to plasmonic enhancement. *J. Photochem. Photobiol. C* **2015**, *24*, 64–82. [CrossRef]

24. Vikrant, K.; Park, C.M.; Kim, K.H.; Kumar, S.; Jeon, E.C. Recent advancements in photocatalyst-based platforms for the destruction of gaseous benzene: Performance evaluation of different modes of photocatalytic operations and against adsorption techniques. *J. Photochem. Photobiol. C* **2019**, *41*, 100316. [CrossRef]

25. Zeng, Y.; Xie, R.; Cao, J.; Chen, Z.; Huang, H. Simultaneous removal of multiple indoor-air pollutants using a combined process of electrostatic precipitation and catalytic decomposition. *Chem. Eng. J.* **2020**, *388*, 124219. [CrossRef]

26. Wang, J.; Deng, H.; Li, X.; Yang, C.; Xia, Y. Visible-light photocatalysis enhanced room-temperature formaldehyde gas sensing by MoS₂/rGO hybrids. *Sens. Actuat. B* **2020**, *304*, 127317. [CrossRef]

27. Magudieshwaran, R.; Ishii, J.; Raja, K.C.N.; Terashima, C.; Pitchaimuthu, S. Green and chemical synthesized CeO₂ nanoparticles for photocatalytic indoor air pollutant degradation. *Mater. Lett.* **2019**, *239*, 40–44. [CrossRef]

28. Dong, X.; Zhang, W.; Sun, Y.; Li, J.; Dong, F. Visible-light-induced charge transfer pathway and photocatalysis mechanism on Bi semimetal@defective BiOBr hierarchical microspheres. *J. Catal.* **2018**, *357*, 41–50. [CrossRef]

29. Tomer, V.K.; Malik, R.; Chaudhary, V.; Mishra, Y.K.; Lin, L. Superior visible light photocatalysis and low-operating temperature VOCs sensor using cubic Ag(0)-MoS₂ loaded g-CN 3D porous hybrid. *Appl. Mater. Today* **2019**, *16*, 193–203. [CrossRef]

30. Kamaei, M.; Rashedi, H.; Dastgheib, S.M.M.; Tasharrofi, S. Comparing Photocatalytic Degradation of Gaseous Ethylbenzene Using N-doped and Pure TiO₂ Nano-Catalysts Coated on Glass Beads under Both UV and Visible Light Irradiation. *Catalysts* **2018**, *8*, 466. [CrossRef]

31. Miao, L.; Xie, Y.; Xia, Y.; Zou, N.; Wang, J. Facile photo-driven strategy for the regeneration of a hierarchical C@MnO₂ sponge for the removal of indoor toluene. *Appl. Surf. Sci.* **2019**, *481*, 404–413. [CrossRef]

32. Enesca, A.; Andronic, L.; Duta, A. Optimization of Opto-Electrical and Photocatalytic Properties of SnO₂ Thin Films Using Zn²⁺ and W⁶⁺ Dopant Ions. *Catal. Lett.* **2012**, *142*, 224–230. [CrossRef]

33. Parrino, F.; Camera-Roda, G.; Loddo, V.; Palmisano, G.; Augugliaro, V. Combination of ozonation and photocatalysis for purification of aqueous effluents containing formic acid as probe pollutant and bromide ion. *Water Res.* **2014**, *50*, 189–199. [CrossRef] [PubMed]

34. Vellingiri, K.; Vikrant, K.; Kumar, V.; Kim, K.H. Advances in thermocatalytic and photocatalytic techniques for the room/low temperature oxidative removal of formaldehyde in air. *Chem. Eng. J.* **2020**, *399*, 125759. [CrossRef]

35. Han, M.; Zhu, S.; Lu, S.; Song, Y.; Yang, B. Recent progress on the photocatalysis of carbon dots: Classification, mechanism and applications. *Nano Today* **2018**, *19*, 201–218. [CrossRef]

36. Destaillats, H.; Sleiman, M.; Sullivan, D.P.; Jacquiod, C.; Molins, L. Key parameters influencing the performance of photocatalytic oxidation (PCO) air purification under realistic indoor conditions. *Appl. Catal. B* **2012**, *128*, 159–170. [CrossRef]

37. Wang, S.; Ang, H.M.; Tade, M.O. Volatile organic compounds in indoor environment and photocatalytic oxidation: State of the art. *Environ. Int.* **2007**, *33*, 694–705. [CrossRef]

38. Mamaghani, A.H.; Haghighat, F.; Lee, C.S. Photocatalytic oxidation technology for indoor environment air purification: The state-of-the-art. *Appl. Catal. B* **2017**, *203*, 247–269. [CrossRef]

39. Guillard, C.; Bui, T.H.; Felix, C.; Moules, V.; Lejeune, P. Microbiological disinfection of water and air by photocatalysis. *C.R. Chimie* **2008**, *11*, 107–113. [CrossRef]

40. Ao, C.H.; Lee, S.C.; Yu, J.Z.; Xu, J.H. Photodegradation of formaldehyde by photocatalyst TiO_2: Effects on the presences of NO, SO_2 and VOCs. *Appl. Catal. B* **2004**, *54*, 41–50. [CrossRef]

41. Kopelovich, J.; Perez, A.L.; Jacobs, N.; Mendelsohn, E.; Keenan, J.J. Screening-level human health risk assessment of toluene and dibutyl phthalate in nail lacquers. *Food Chem. Toxicol.* **2015**, *81*, 46–53. [CrossRef] [PubMed]

42. Gericke, C.; Hanke, B.; Beckmann, G.; Baltes, M.M. Multicenter field trial on possible health effects of toluene: III. Evaluation of effects after long-term exposure. *Toxicology* **2001**, *168*, 185–209. [CrossRef]

43. Jeon, J.; Park, J.H.; Wi, S.; Yun, B.Y.; Kim, S. Field study on the improvement of indoor air quality with toluene adsorption finishing materials in an urban residential apartment. *Environ. Pollut.* **2020**, *261*, 114137. [CrossRef] [PubMed]

44. Chen, J.; Zhang, X.; Shi, X.; Bi, F.; Yang, Y.; Wang, Y. Synergistic effects of octahedral TiO_2-MIL-101(Cr) with two heterojunctions for enhancing visible-light photocatalytic degradation of liquid tetracycline and gaseous toluene. *J. Colloid Interface Sci.* **2020**, *579*, 37–49. [CrossRef] [PubMed]

45. Zou, X.; Dong, Y.; Ke, J.; Ge, H.; Chen, D.; Sun, H.; Cui, Y. Cobalt monoxide/tungsten trioxide p-n heterojunction boosting charge separation for efficient visible-light-driven gaseous toluene degradation. *Chem. Eng. J.* **2020**, *400*, 125919. [CrossRef]

46. Cui, W.; Li, J.; Chen, L.; Dong, X.; Wang, H.; Sheng, J.; Sun, Y.; Zhou, Y.; Dong, F. Nature-inspired $CaCO_3$ loading TiO_2 composites for efficient and durable photocatalytic mineralization of gaseous toluene. *Sci. Bull.* **2020**, *65*, 1626–1634. [CrossRef]

47. Zhao, Y.; Ma, L.; Chang, W.; Huang, Z.; Feng, X.; Qi, X.; Li, Z. Efficient photocatalytic degradation of gaseous *N,N*-dimethylformamide in tannery waste gas using doubly open-ended Ag/TiO_2 nanotube array membranes. *Appl. Surf. Sci.* **2018**, *444*, 610–620. [CrossRef]

48. Wang, L.; Gao, X.; Cheng, Y.; Zhang, X.; Wang, G.; Zhang, Q.; Su, J. TiO_2@MgAl-layered double hydroxide with enhanced photocatalytic activity towards degradation of gaseous toluene. *J. Photochem. Photobiol. A* **2019**, *369*, 44–53. [CrossRef]

49. Liu, Y.; Xie, C.; Li, H.; Chen, H.; Zou, T.; Zeng, D. Improvement of gaseous pollutant photocatalysis with WO_3/TiO_2 heterojunctional-electrical layered system. *J. Hazard. Mater.* **2011**, *196*, 52–58. [CrossRef]

50. Reingruber, H.; Pontel, L.B. Formaldehyde metabolism and its impact on human health. *Curr. Opin. Toxicol.* **2018**, *9*, 28–34. [CrossRef]

51. Ferreira, J.R.; Rezende, L.C.; Barbosa, A.S.; Carvalho, P.; Carvalho, A.A. Economic, human and environmental health benefits of replacing formaldehyde in the preservation of corpses. *Ecotoxicol. Environ. Safety* **2017**, *145*, 490–495. [CrossRef] [PubMed]

52. Huang, C.; Liu, W.; Cai, J.; Wang, X.; Sun, C. Household formaldehyde exposure and its associations with dwelling characteristics, lifestyle behaviours, and childhood health outcomes in Shanghai, China. *Build. Environ.* **2017**, *125*, 143–152. [CrossRef]

53. Noisel, N.; Bouchard, M.; Carrier, G. Evaluation of the health impact of lowering the formaldehyde occupational exposure limit for Quebec workers. *Regul. Toxicol. Pharm.* **2007**, *48*, 118–127. [CrossRef] [PubMed]

54. Wang, Z.; Yu, H.; Xiao, Y.; Zhang, L.; Guo, L.; Zhang, L.; Dong, X. Free-standing composite films of multiple 2D nanosheets: Synergetic photothermocatalysis/photocatalysis for efficient removal of formaldehyde under ambient condition. *Chem. Eng. J.* **2020**, *394*, 125014. [CrossRef]

55. Xia, S.; Zhang, G.; Meng, Y.; Yang, C.; Ni, Z.; Hu, J. Kinetic and mechanistic analysis for the photodegradation of gaseous formaldehyde by core-shell CeO_2@LDHs. *Appl. Catal. B* **2020**, *278*, 119266. [CrossRef]

56. Armenta-Reséndiz, M.; Ríos-Leal, E.; Rivera-García, M.T.; López-Rubalcava, C.; Cruz, S.L. Structure-activity study of acute neurobehavioral effects of cyclohexane, benzene, m-xylene, and toluene in rats. *Toxicol. Appl. Pharm.* **2019**, *376*, 38–45. [CrossRef]

57. Singh, M.P.; Mishra, M.; Sharma, A.; Shukla, A.K.; Kar Chowdhuri, D. Genotoxicity and apoptosis in Drosophila melanogaster exposed to benzene, toluene and xylene: Attenuation by quercetin and curcumin. *Toxicol. Appl. Pharm.* **2011**, *253*, 14–30. [CrossRef]

58. Lee, E.; Ahn, S.; Jin, S.H.; Lee, M.; Noh, M. CXCL14 downregulation in human keratinocytes is a potential biomarker for a novel in vitro skin sensitization test. *Toxicol. Appl. Pharm.* **2020**, *386*, 114828. [CrossRef]

59. Jenkins, L.J.; Jones, R.A.; Siegel, J. Long-term inhalation screening studies of benzene, toluene, o-xylene, and cumene on experimental plants. *Toxicol. Appl. Pharm.* **1970**, *16*, 818–823. [CrossRef]

60. Lin, W.; Xie, X.; Wang, X.; Wang, Y.; Segets, D.; Sun, J. Efficient adsorption and sustainable degradation of gaseous acetaldehyde and o-xylene using rGO-TiO_2 photocatalyst. *Chem. Eng. J.* **2018**, *349*, 708–718. [CrossRef]

61. Edokpolo, B.; Yu, Q.J.; Connell, D. Use of toxicant sensitivity distributions (TSD) for development of exposure guidelines for risk to human health from benzene. *Environ. Pollut.* **2019**, *250*, 386–396. [CrossRef] [PubMed]

62. Bahadar, H.; Mostafalou, S.; Abdollahi, M. Current understandings and perspectives on non-cancer health effects of benzene: A global concern. *Toxicol. Appl. Pharm.* **2014**, *276*, 83–94. [CrossRef] [PubMed]

63. Edokpolo, B.; Yu, Q.J.; Connell, D. Health risk characterization for exposure to benzene in service stations and petroleum refineries environments using human adverse response data. *Toxicol. Rep.* **2015**, *2*, 917–927. [CrossRef] [PubMed]

64. Yang, L.; Wang, F.; Shu, C.; Liu, P.; Zhang, W.; Hu, S. TiO_2/porous cementitious composites: Influences of porosities and TiO_2 loading levels on photocatalytic degradation of gaseous benzene. *Constr. Build. Mater.* **2017**, *150*, 774–780. [CrossRef]

65. Tri, N.L.; Duc, D.S.; Thuan, D.V.; Tahtamouni, T.A.; Pham, T.D.; Tran, D.T.; Phuong Le Chi, N.T.; Nguyen, V.N. Superior photocatalytic activity of Cu doped $NiWO_4$ for efficient degradation of benzene in air even under visible radiation. *Chem. Phys.* **2019**, *525*, 110411. [CrossRef]

66. Hu, Y.; Li, D.; Zheng, Y.; Chen, W.; He, Y.; Shao, Y.; Fu, X.; Xiao, G. $BiVO_4$/TiO_2 nanocrystalline heterostructure: A wide spectrum responsive photocatalyst towards the highly efficient decomposition of gaseous benzene. *Appl. Catal. B* **2011**, *104*, 30–36. [CrossRef]

67. Wang, J.; Li, H.; Meng, S.; Zhang, L.; Fu, X.; Chen, S. One-pot hydrothermal synthesis of highly efficient SnO_x/Zn_2SnO_4 composite photocatalyst for the degradation of methyl orange and gaseous benzene. *Appl. Catal. B* **2017**, *200*, 19–30. [CrossRef]

68. Chun, H.H.; Lee, j.Y.; Jo, W.K. Photocatalysis of low-concentration gaseous organic pollutants over electrospun iron-doped titanium dioxide nanofibers. *Solid State Sci.* **2013**, *25*, 103–109. [CrossRef]

69. Cheng, Z.W.; Feng, L.; Chen, J.M.; Yu, J.M.; Jiang, Y.F. Photocatalytic conversion of gaseous ethylbenzene on lanthanum-doped titanium dioxide nanotubes. *J. Hazard. Mater.* **2013**, *254*, 354–363. [CrossRef]

70. Delikhoon, M.; Fazlzadeh, M.; Sorooshian, A.; Baghani, A.N.; Barkhordari, A. Characteristics and health effects of formaldehyde and acetaldehyde in an urban area in Iran. *Environ. Pollut.* **2018**, *242*, 938–951. [CrossRef]

71. Tian, X.; Shen, Z.; Zhou, Y.; Wang, K. Inhibition on biological acidification and microbial community by high-strength acetaldehyde. *Process. Saf. Environ.* **2020**, *143*, 231–238. [CrossRef]

72. Fan, G.; Xie, J.; Yoshino, H.; Zhang, H.; Liu, J. Concentration characteristics of gaseous carbonyl compounds in urban houses in two different climatic zones of China and health risk assessment for schoolchildren. *Sustain. Cities Soc.* **2020**, *60*, 102270. [CrossRef]

73. Lachenmeier, D.W.; Salaspuro, M. ALDH2-deficiency as genetic epidemiologic and biochemical model for the carcinogenicity of acetaldehyde. *Regul. Toxicol. Pharm.* **2017**, *86*, 128–136. [CrossRef] [PubMed]

74. Zeng, Q.; Xie, X.; Wang, X.; Lu, G.; Li, H.; Lee, S.C.; Sun, J. New insights into the synergistic effect of active radicals and adsorptive ability on the photodegradation of gaseous acetaldehyde over reduced graphene Oxide/P25 composite. *J. Hazard. Mater.* **2019**, *380*, 120814. [CrossRef]

75. Zeng, Q.; Wang, X.; Xie, X.; Lu, G.; Wang, Y.; Lee, S.C.; Sun, J. TiO_2/TaS_2 with superior charge separation and adsorptive capacity to the photodegradation of gaseous acetaldehyde. *Chem. Eng. J.* **2020**, *379*, 122395. [CrossRef]

76. Zeng, Q.; Xie, X.; Wang, X.; Wang, Y.; Lu, G.; Pui, D.Y.H.; Sun, J. Enhanced photocatalytic performance of $Ag@TiO_2$ for the gaseous acetaldehyde photodegradation under fluorescent lamp. *Chem. Eng. J.* **2018**, *341*, 83–92. [CrossRef]

77. Hu, Y.; Xie, X.; Wang, X.; Wang, Y.; Zeng, Y.; Pui, D.Y.H.; Sun, J. Visible-Light Upconversion Carbon Quantum Dots Decorated TiO_2 for the Photodegradation of Flowing Gaseous Acetaldehyde. *Appl. Surf. Sci.* **2018**, *440*, 266–274. [CrossRef]

78. Thevenet, F.; Guaitell, O.; Puzenat, E.; Herrmann, J.M.; Rousseau, A.; Guillard, C. Oxidation of acetylene by photocatalysis coupled with dielectric barrier discharge. *Catal. Today* **2007**, *122*, 186–194. [CrossRef]

79. Enesca, A.; Yamaguchi, Y.; Terashima, C.; Fujishima, A.; Nakata, K.; Duta, A. Enhanced UV–Vis photocatalytic performance of the $CuInS_2/TiO_2/SnO_2$ hetero-structure for air decontamination. *J. Catal.* **2017**, *350*, 174–181. [CrossRef]

80. Chun, H.H.; Jo, W.K. Adsorption and photocatalysis of 2-ethyl-1-hexanol over graphene oxide–TiO_2 hybrids post-treated under various thermal conditions. *Appl. Catal. B* **2016**, *180*, 740–750. [CrossRef]

81. Costa Filho, B.M.; Araujo, A.L.P.; Silva, G.V.; Boaventura, R.A.R.; Dias, M.M.; Lopes, J.C.B.; Vilar, V.J.P. Intensification of heterogeneous TiO_2 photocatalysis using an innovative micro-meso-structured-photoreactor for n-decane oxidation at gas phase. *Chem. Eng. J.* **2017**, *310*, 331–341. [CrossRef]

82. McKee, R.H.; Nessel, C.S.; Carrillo, J.C. An investigation of the acute central nervous system effects of n-decane. *Regul. Toxicol. Pharmacol.* **2019**, *107*, 104421. [CrossRef] [PubMed]

83. Kjærgaard, S.; Mølhave, L.; Pedersen, O.F. Human reactions to indoor air pollutants: N-decane. *Environ. Int.* **1989**, *15*, 273–282. [CrossRef]

84. Akinola, J.O.; Olawusi-Peters, O.O.; Apkambang, V.O. Human health risk assessment of TPHs in brackish water prawn (Nematopalaemon hastatus, AURIVILLUS, 1898). *Heliyon* **2020**, *6*, e03234. [CrossRef] [PubMed]

85. Yu, Q.; Chen, J.; Li, Y.; Wen, M.; Liu, H.; Li, G.; An, T. In-situ decoration of metallic Bi on BiOBr with exposed (110) facets and surface oxygen vacancy for enhanced solar light photocatalytic degradation of gaseous n-hexane. *Chinese J. Catal.* **2020**, *41*, 1603–1612. [CrossRef]

86. Mohseni, M. Gas phase trichloroethylene (TCE) photooxidation and byproduct formation: Photolysis vs. titania/silica based photocatalysis. *Chemosphere* **2005**, *59*, 335–342. [CrossRef]

87. Li, M.; Li, Y.; Chen, F.; Lin, X.; Feng, Q. Electrically enhanced photocatalysis for gas-phase benzaldehyde degradation by ordered mesoporous titania/conductive carbon felts. *Electrochim. Acta* **2016**, *216*, 517–527. [CrossRef]

88. Sayed, M.; Arooj, A.; Shah, N.S.; Khan, J.A.; Shah, L.A.; Rehman, F.; Arandiyan, H.; Khan, A.M.; Khan, A.R. Narrowing the band gap of TiO_2 by co-doping with Mn^{2+} and Co^{2+} for efficient photocatalytic degradation of enoxacin and its additional peroxidase like activity: A mechanistic approach. *J. Molec. Liq.* **2018**, *272*, 403–412. [CrossRef]

89. Gul, I.; Sayed, M.; Shah, N.S.; Khan, J.A.; Polychronopoulou, K.; Iqbal, J.; Rehman, F. Solar light responsive bismuth doped titania with Ti^{3+} for efficient photocatalytic degradation of flumequine: Synergistic role of peroxymonosulfate. *Chem. Eng. J.* **2020**, *384*, 123255. [CrossRef]

90. Khan, J.A.; Sayed, M.; Shah, N.S.; Khan, S.; Zhang, Y.; Boczkaj, G.; Khan, H.M.; Dionysiou, D.D. Synthesis of eosin modified TiO_2 film with co-exposed {001} and {101} facets for photocatalytic degradation of para-aminobenzoic acid and solar H_2 production. *App. Catal. B Environ.* **2019**, *265*, 118557. [CrossRef]